

NUMERICAL STUDY ON DYNAMIC STALL OF FIGHTER AIRCRAFT AT HIGH ANGLE OF ATTACK USING DYNAMIC IMPROVED DELAYED DETACHED EDDY SIMULATION

Huiyue Wang[1,2], Tianyu Lin[1,2], Gang Wang[1,2*],Lincheng Xu[1,2]

[1] School of Aeronautics, Northwestern Polytechnical University, Xi'an 710072, China
[2] National Key Laboratory of Aircraft Configuration Design, Xi'an 710072, China
* Corresponding Author: wanggang@nwpu.edu.cn

Abstract

Dynamic stall is a complex unsteady flow phenomenon that fighter aircraft must face when performing stall maneuvers at a large angle of attack. It is directly related to flight performance, maneuverability, and flight safety. In current engineering practice, the dynamic stall of fighter aircraft is typically simulated using Reynolds-Averaged Navier-Stokes (RANS) methods. However, due to turbulence-modeling, time averaging can suppress key unsteady separation mechanisms, RANS often fails to accurately capture the vortex evolution in dynamic stalling of a fighter aircraft. To address these limitations, this study employs a high-resolution Dynamic Improved Delayed Detached-Eddy Simulation (DynIDDES) together with a three-dimensional Navier-Stokes solver on unstructured hybrid meshes, and a standard wind-tunnel fighter model is selected as the test case. The simulation includes static simulation at attack angle of -5° to 90° compared with wind tunnel data and dynamic stall simulation at longitudinal maneuver. The results indicate that compared to RANS, DynIDDES method significantly improves the accuracy of aerodynamic prediction at high angles of attack. It captures critical unsteady flow characteristics, such as asymmetric separation and vortex breakup, and its predictions remain highly consistent with wind tunnel data. Furthermore, the DynIDDES method also accurately predicts the aerodynamic characteristics of dynamic stall during the longitudinal maneuver of fighter aircraft. Specifically, dynamic stall significantly strengthens the strake vortex and delays its breakup, thereby substantially increasing the lift and drag coefficients.

Keywords: High-angle-of-attack flow, Dynamic stall, Dynamic improved delayed detached-eddy simulation

1. General Introduction

High angle-of-attack maneuverability represents a core capability of modern high-performance fighters. Typical post-stall maneuvers such as the Cobra maneuver rely on complex high-angle separated flows to achieve rapid attitude changes and gain tactical superiority [1,2]. Such maneuver performance has become one of the important indicators for the aerodynamic layout design of advanced fighter aircraft [3]. However, during high angle of attack, especially rapid pitch maneuvers, the flow field will exhibit complex unsteady phenomena such as strong separation, leading-edge vortex evolution, vortex breakup and asymmetric instability. Distinct from static stall, the flow exhibits prominent unsteady characteristics and dynamic hysteresis, along with separation lag, large-scale vortex motion and shedding. These phenomena induce remarkable instantaneous fluctuations in aerodynamic forces and pitching moment [4,5]. While the evolution of these intricate flow structures dictates an aircraft's aerodynamic performance and handling qualities, it also imposes critical impacts on flight safety and control behavior.

Flight and wind-tunnel experiments provide valuable aerodynamic data for high-angle-of-attack flows [6]. However, the acquisition of detailed three-dimensional unsteady flow information remains challenging because of measurement limitations, cost, and operational constraints. As a result, high-fidelity numerical simulations have become an important tool for investigating flow physics and aerodynamic mechanisms [7-10]. Major numerical methods include RANS, LES, DNS and hybrid RANS/LES. RANS is efficient but limited by inherent over-modelling when predicting complex

separated flows at high angles of attack [11]. LES has high accuracy but incurs unaffordable computational cost for engineering scenarios [12,13]. DES series methods well balance efficiency and resolution [14-16]. The employed DynIDDES enhances the capacity to resolve unsteady turbulent structures through a dynamic subgrid model, which delivers accurate predictions for high-angle-of-attack complex flows at an acceptable computational expense [17-19].

Despite these developments, accurately predicting three-dimensional high-angle-of-attack separated flows in complex fighter configurations remains challenging. Extensive numerical studies have been performed on high-angle-of-attack flows. RANS serves as the mainstream tool for engineering aerodynamic analysis, yet its excessive turbulence modelling suppresses unsteady flow separation and cannot accurately reproduce the evolution of vortex structures [4]. Hybrid RANS/LES methods including DES and IDDES achieve higher accuracy for separated flows, but their performance still needs further improvement for complex unsteady flow problems [20-22]. As an enhanced hybrid scheme developed on the basis of IDDES, DynIDDES optimizes the near-wall treatment and turbulence resolution, enabling more reliable prediction of large-scale vortex evolution and flow separation under strong adverse pressure gradients. However, systematic applications and performance assessments of this method on three-dimensional high-angle-of-attack flows around fighter configurations remain limited.

Based on the above background, this paper adopts the in-house hybrid unstructured mesh three-dimensional Navier-Stokes solver HUNS3D [23] and uses the DynIDDES method to conduct large angle-of-attack static and dynamic stall numerical simulations on a typical fighter wind tunnel standard model. First, by combining wind tunnel test data, the prediction accuracy of RANS and DynIDDES methods for separated flow and aerodynamic loads is compared. Then, simulations of rapid longitudinal pitching are carried out to analyze the evolution of unsteady flow fields and aerodynamic responses, and clarify the influence of vortex structures on dynamic aerodynamic characteristics.

2. Numerical Method

2.1 Baseline Solver

This paper employs a three-dimensional Navier-Stokes equation solver (HUNS3D) based on a hybrid unstructured mesh. This solver uses the finite volume method to discretize and solve the integral form of the Navier-Stokes (N-S) equations, demonstrating its ability to handle complex geometries and multi-scale flow problems. The solver has demonstrated robust performance in simulations of complex turbulent structures, strongly unsteady separated flows, and multi-scale vortex evolution [24,25].

$$\frac{\partial}{\partial t}\iiint_{\Omega}\boldsymbol{Q}dV+\iint_{\partial\Omega}\boldsymbol{F}(\boldsymbol{Q},\boldsymbol{V}_{\text{grid}})\cdot\boldsymbol{n}dS=\iint_{\partial\Omega}\boldsymbol{G}(\boldsymbol{Q})\cdot\boldsymbol{n}dS \tag{1a}$$

$$\boldsymbol{F}(\boldsymbol{Q})\cdot\boldsymbol{n}=\left[\left(\boldsymbol{V}-\boldsymbol{V}_{\text{grid}}\right)\cdot\boldsymbol{n}\right]\begin{pmatrix}\overline{\rho}\\ \overline{\rho}\tilde{u}\\ \overline{\rho}\tilde{v}\\ \overline{\rho}\tilde{w}\\ \overline{\rho}\tilde{H}\end{pmatrix}+\overline{p}\begin{pmatrix}0\\ n_x\\ n_y\\ n_z\\ 0\end{pmatrix} \tag{1b}$$

$$\boldsymbol{G}(\boldsymbol{Q})\cdot\boldsymbol{n}=\begin{pmatrix}0\\ \overline{\tau}_{xx}\\ \overline{\tau}_{yx}\\ \overline{\tau}_{zx}\\ \tilde{u}\overline{\tau}_{xx}+\tilde{v}\overline{\tau}_{xy}+\tilde{w}\overline{\tau}_{xz}-\overline{q}_x\end{pmatrix}n_x+\begin{pmatrix}0\\ \overline{\tau}_{xy}\\ \overline{\tau}_{yy}\\ \overline{\tau}_{zy}\\ \overline{\tau}_{yx}+\overline{v}\overline{\tau}_{yy}+\tilde{w}\overline{\tau}_{yz}-\overline{q}_y\end{pmatrix}n_y+\begin{pmatrix}0\\ \overline{\tau}_{xz}\\ \overline{\tau}_{yz}\\ \overline{\tau}_{zz}\\ \tilde{u}\overline{\tau}_{zx}+\tilde{v}\overline{\tau}_{zy}+\tilde{w}\overline{\tau}_{zz}-\overline{q}_z\end{pmatrix}n_z \tag{1c}$$

Ω is the unit normal vector, $\partial\Omega$ representing the boundary of the control volume, $\boldsymbol{V_{grid}}$ is the grid motion velocity, and $\boldsymbol{n}$ is the unit normal vector of the control volume surface.

$\mathbf{Q}=(\bar{\rho}\quad \bar{\rho}\tilde{u}\quad \bar{\rho}\tilde{v}\quad \bar{\rho}\tilde{w}\quad \bar{\rho}\tilde{E})^{\mathrm{T}}$ are conserved variables, $\bar{*}$ represents the filter quantity, and $\tilde{*}$ represents the Favre filter quantity. ρ、u、v、w、p and E represent the fluid density, velocity component, static pressure, and total energy per unit volume, respectively. $\tau_{ij}=\tau_{ij}^{1}-\bar{\rho}\tilde{R}_{ij}$ is the sum of the laminar viscous stress and turbulent stress tensors, obtained from Newton's law of viscosity and the turbulence model, respectively. $\bar{q}_k=\bar{q}_k^{1}+\bar{q}_k^{\mathrm{t}}$ represents the sum of the laminar heat flux and the turbulent heat flux.

2.2 Turbulence modeling

This paper employs a combination of the Shear Stress Transport (SST) model and the DynIDDES method for turbulence modeling. The DynIDDES method, developed from the IDDES framework, introduces a dynamic Smagorinsky subgrid-scale model into the LES region to adaptively adjust the local flow state, thereby improving the resolution capability of turbulent structure analysis in the off-wall region while maintaining modeling accuracy in the near-wall region.

The governing equations of the SST model are as follows:

$$\frac{\partial}{\partial t}(\bar{\rho}\tilde{k})+\frac{\partial}{\partial x_k}(\bar{\rho}\tilde{u}_k\tilde{k})=(-2\mu_t\tilde{S}_{ij}^{*}+2/3\bar{\rho}\tilde{k}\delta_{ij})\tilde{u}_{i,j}-\beta_k\bar{\rho}\omega k+\frac{\partial}{\partial x_k}\left[(\bar{\mu}+\sigma_k u_t)\frac{\partial\tilde{k}}{\partial x_k}\right] \tag{2}$$

$$\frac{\partial}{\partial t}(\bar{\rho}\omega)+\frac{\partial}{\partial x_k}(\bar{\rho}\tilde{u}_k\omega)=\frac{\gamma}{\nu_t}\bar{R}_{ij}\tilde{u}_{i,j}-\beta_\omega\rho\omega^2+\frac{\partial}{\partial x_k}\left[(\bar{\mu}+\sigma_\omega u_t)\frac{\partial\omega}{\partial x_k}\right]+2(1-F_1)\frac{\rho\sigma_{\omega2}}{\omega}\frac{\partial\tilde{k}}{\partial x_k}\frac{\partial\omega}{\partial x_k} \tag{3}$$

Where, β_k, σ_ω and β_ω are constants in the SST model.

To ensure a smooth transition between the k-ε model and the k-ω model, a mixture function is introduced:

$$\varphi=F_1\varphi_1+(1-F_1)\varphi_2 \tag{4}$$

Where φ represents the general model variable, and *F1* is the mixture function.

In the DynIDDES method, the characteristic length scale in the dissipation term is replaced with the IDDES mixing length, and a dynamic subgrid model is introduced in the LES region to achieve adaptive coupling between the RANS and LES regions. This dynamic modeling strategy can adaptively adjust the subgrid model parameters according to local flow characteristics, thereby improving the predictive ability of complex unsteady flows. Its turbulent kinetic energy dissipation term can be expressed as:

$$\beta_k\rho k\omega=\frac{\rho k^{3/2}}{l_{\mathrm{IDDES}}} \tag{5}$$

wherein, the IDDES blending length is defined as:

$$l_{\mathrm{IDDES}}=\bar{f}_{\mathrm{d}}(1+f_{\mathrm{e}})l_{\mathrm{RANS}}+(1-\bar{f}_{\mathrm{d}})l_{\mathrm{LES}} \tag{6}$$

In the formula, l_{RANS} and l_{LES} represent the feature length scales of the RANS region and LES region, respectively.

In the RANS region, the feature length scale is defined as:

$$l_{\mathrm{RANS}}=\sqrt{\tilde{k}}/(\beta_k\omega) \tag{7}$$

In the LES region, the feature length scale is:

$$l_{LES}=C_{DES}\Delta \tag{8}$$

where Δ is the local mesh scale.

Key parameters in the DynIDDES method are determined using a dynamic method:

$$C_{DES} = C_k C_s \tag{9}$$

The model coefficients are dynamically evaluated using the Germano identity:

$$L_{ij} = C_s^2 M_{ij} \tag{10a}$$

$$L_{ij} = \overline{\tilde{u}_i \tilde{u}_j} - \overline{\tilde{u}}_i \overline{\tilde{u}}_j \tag{10b}$$

$$M_{ij} = 2\Delta^2 |\tilde{S}| \tilde{S}_{ij} - 2\overline{\Delta}^2 |\overline{S}| \overline{S}_{ij} \tag{10c}$$

The model coefficient is obtained through a least-squares procedure:

$$C_s^2 = \frac{\langle L_{ij} M_{ij} \rangle}{\langle M_{ij} M_{ij} \rangle} \tag{11}$$

where, $\langle \cdot \rangle$ represents a volume-weighted average of adjacent cells. When $C_s^2 < 0$, to ensure numerical stability, it is truncated to zero.

3. Description of cases

To evaluate the resolution capability of the DynIDDES method for unsteady separated flow at high angle of attack of fighters, this paper carries out numerical simulations on a scaled simplified fighter model and validates the results against wind tunnel test data. The geometric configuration of the model is shown in Fig. 1, and detailed geometric dimensions are given in reference [26]. The model reference area S = 0.0432 m², reference chord length c = 0.1222 m, reference span b = 0.394 m, fuselage length L = 0.52 m, and the moment reference point coordinate is (0.3394, 0.0, -0.01510556) m. This paper conducts numerical simulations of three typical high angle of attack conditions under the conditions of free-stream Mach number Ma = 0.5 and Reynolds number Re = 1.19×10⁶ (based on reference chord length), namely, static stall at fixed angle of attack, dynamic stall with longitudinal forced pitch. The angle of attack range is -5° to 90°. The surface mesh, computational domain mesh, and boundary conditions of the model are shown in Fig. 2 and 3, respectively. The number of surface meshes is approximately 2.8×10^5, and the total number of computational domain meshes is approximately 3.2×10^7. The height of the first near-wall cell is 1.0×10^{-6} m, corresponding to y^+ of approximately 1.0. In the present simulations, temporal discretization is performed using a second-order implicit dual time-stepping approach with a physical time step of $\Delta t \approx 3 \times 10^{-6}$ s. Spatial discretization adopts the Roe flux scheme combined with the Venkatakrishnan flux limiter for convective terms, while viscous terms are solved via the second-order central difference scheme. To evaluate the numerical performance of the improved hybrid method, comparative calculations are conducted using both the SST-RANS and SST-DynIDDES frameworks. The primary objective is to quantify the capability of the DynIDDES method in predicting high angle-of-attack flow separation, unsteady vortex evolution, and post-stall aerodynamic responses of fighter aircraft.

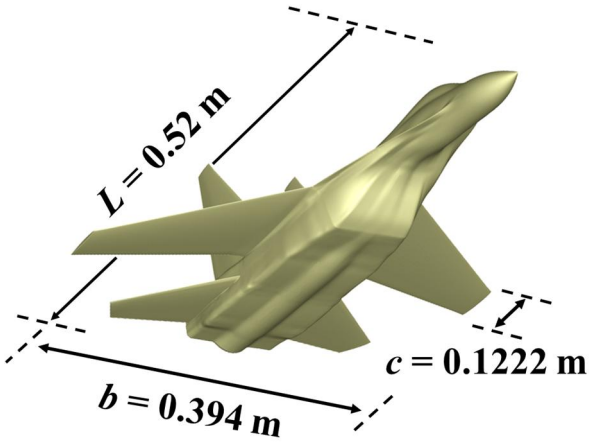


Fig. 1 Geometric model parameters.

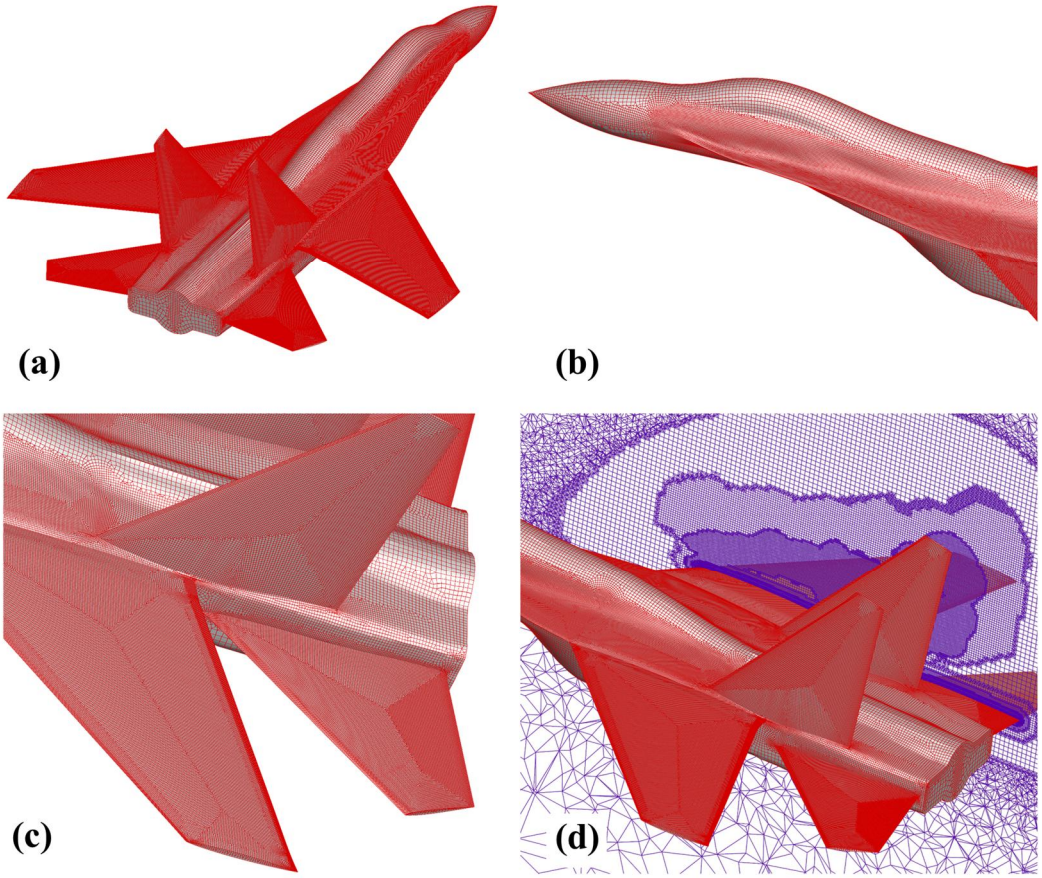


Fig. 2 Fighter model computational mesh. a: Full aircraft surface mesh; b: Leading strake wing; c: Main wing and tail wing; d: Wing section.

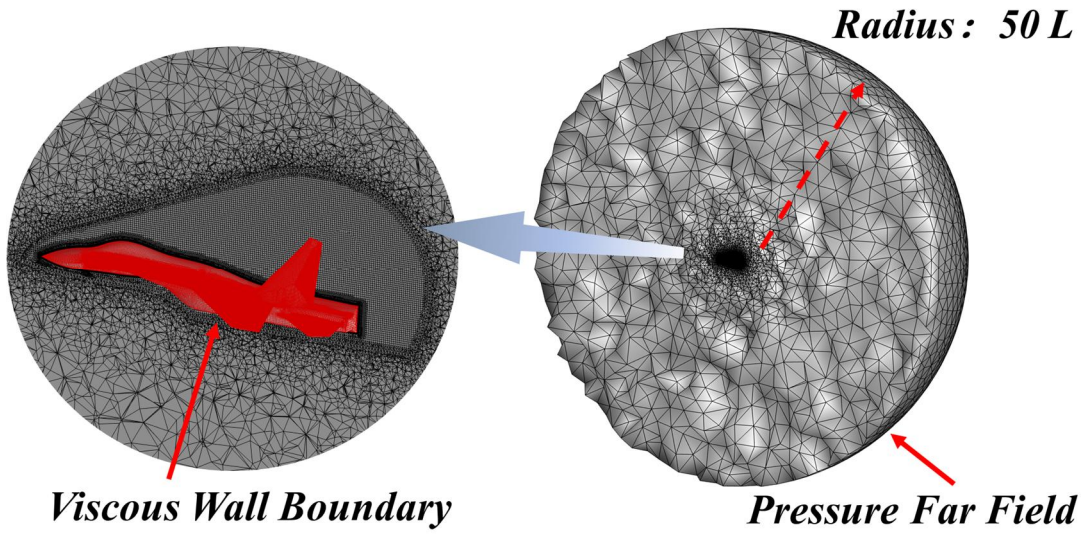


Fig. 3 Schematic diagram of computational domain and boundary conditions.

4. Results and Discussion

In this chapter, numerical results from the RANS and DynIDDES methods are validated and analyzed using wind tunnel test data. Static simulations over a wide angle-of-attack range are first performed to evaluate the prediction accuracy of aerodynamic coefficients and characterize aerodynamic features as well as vortex evolution. Based on the static analysis, dynamic simulations with longitudinal forced pitching motion are further conducted to investigate the aerodynamic hysteresis caused by dynamic stall, and reveal differences in vortex structure resolution between static and dynamic operating conditions.

4.1 Fixed-Angle-of-Attack Flow Simulation

This section focuses on the aerodynamic performance of the fighter model under high angle-of-attack conditions. Static numerical simulations spanning a broad range of angles of attack are carried out using the RANS and DynIDDES methods, aiming to characterize the evolution of aerodynamic coefficients and flow vortex structures. Numerical predictions are further validated against available wind tunnel experimental data to assess the accuracy of the two numerical methods.

Fig. 4 shows the variation of lift coefficient C_L, drag coefficient C_D, and pitching moment coefficient C_{my} calculated by the RANS and DynIDDES methods with angle of attack, and compares them with experimental results. As shown in Fig. 4, both methods can predict the static aerodynamic coefficient variation well, and the numerical results agree well with the experimental data, with no significant differences between the methods. However, as the angle of attack gradually increases and the flow approaches stall, significant differences begin to appear in the prediction results of the two methods. The RANS method slightly advances the prediction of the peak lift position and shows some deviation in characterizing the drag growth trend at large angles of attack; simultaneously, its pitching moment decrease trend is more gradual than the experimental results, failing to fully reflect the rapid rearward movement of the aerodynamic center. In contrast, the DynIDDES method's prediction results for the peak lift position, drag growth slope, and pitching moment abrupt change interval are closer to the experimental data, indicating its better simulation capability for complex separated flows.

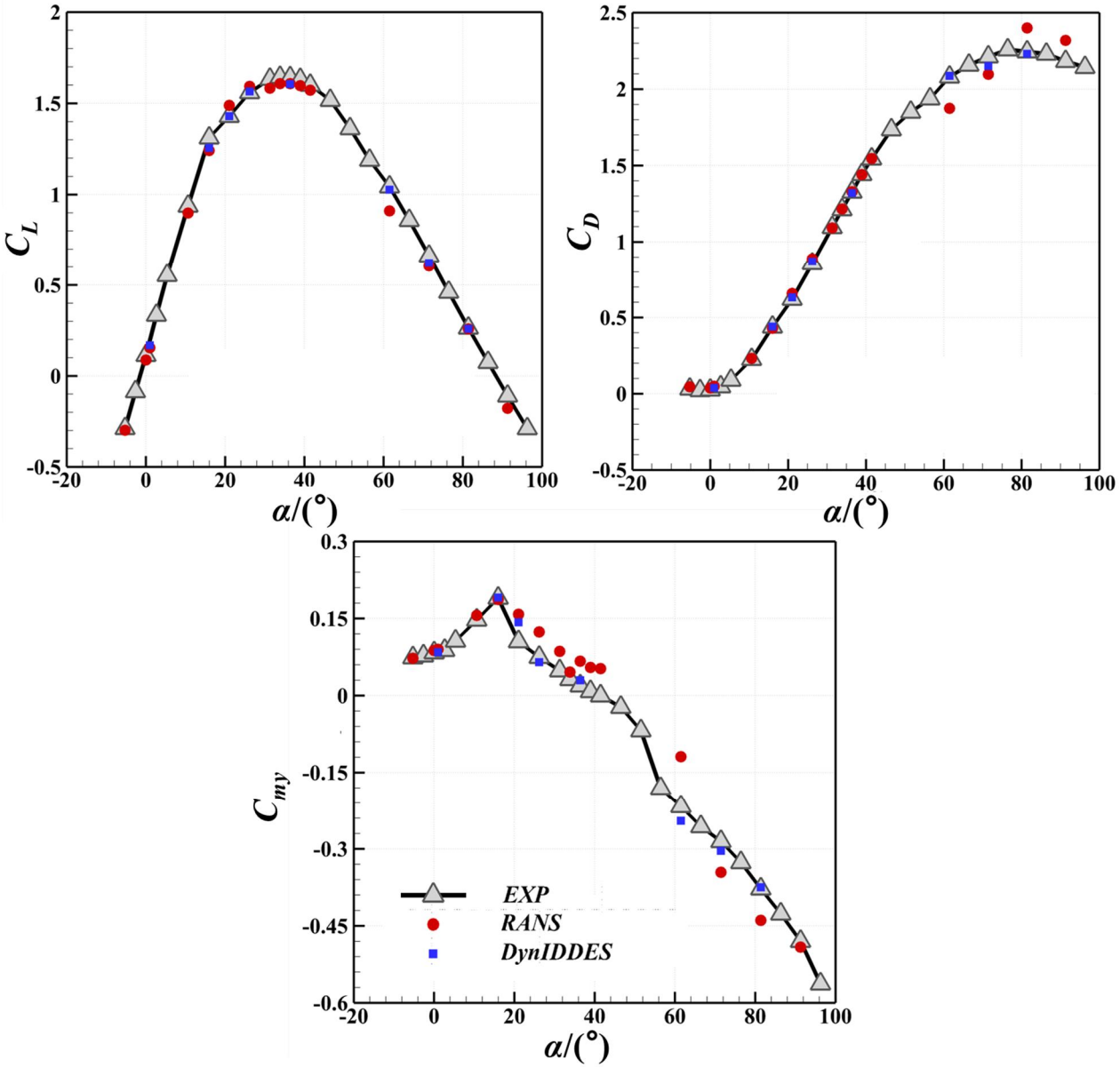


Fig. 4 Comparison of aerodynamic forces and moment coefficients of RANS and DynIDDES at different angles of attack.

To further analyze the flow physics mechanism underlying the prediction differences between the two numerical methods, three typical angles of attack (15.96°, 21.04°, and 26.196°) are selected for vortex field analysis. In this work, the Rortex (also named Liutex) vortex identification method proposed by Liu[27] is adopted to extract real vortical structures. Different from traditional vortex criteria such as the Q criterion, Rortex can decompose vorticity into a rigid rotational part and a pure shear part via the velocity gradient tensor decomposition:

$$\vec{w} = \vec{R} + \vec{S} \tag{12}$$

Where $\vec{w}$ denotes the vorticity vector, $\vec{R}$ represents the Rortex vector describing local rigid rotation, and $\vec{S}$ refers to the pure shear vector. The magnitude of the Rortex scalar equals twice the local fluid rotational angular velocity, which effectively eliminates shear contamination and avoids false vortex identification induced by boundary-layer shear motion.

In this study, the Rortex iso-surface threshold is set to 40 to filter trivial weak-scale vortices and only retain dominant large-scale separated vortices. The visualized vortex distributions are shown in Fig. 5.

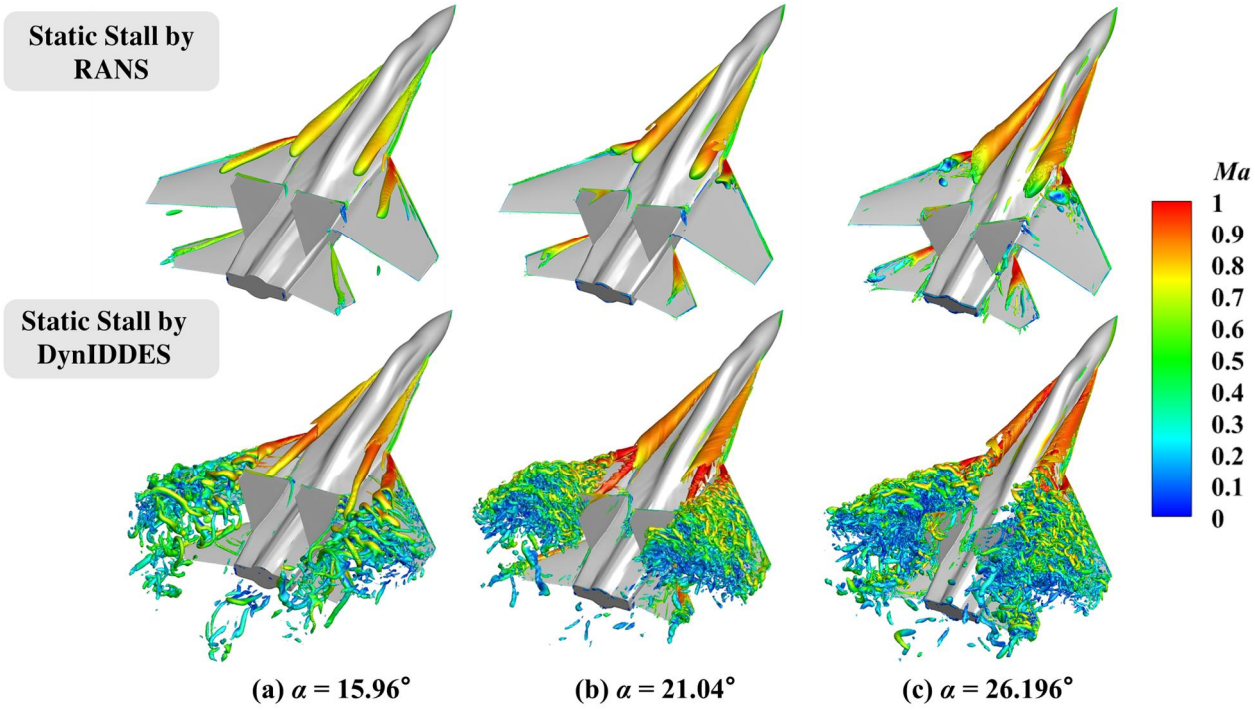


Fig. 5 Comparison of flow field structures in RANS and DynIDDES at different angles of attack. (Rortex = 40)

At an angle of attack of 15.96°, local flow separation and initial vortex structures have already appeared at the leading edge of the wing, while the strake vortex remains intact with no obvious breakdown. Under this condition, RANS and DynIDDES both well reproduce the overall structure of the leading-edge vortex, and their predictions show little difference. As the angle of attack increases to 21.04°, the leading-edge separated vortex gradually intensifies and begins to show significant instability. DynIDDES can clearly resolve flow structures such as vortex entrainment, local vortex breakdown and undulations in the separated shear layer. In comparison, RANS produces severe numerical smoothing, leading to mild spatial variations of vortex structures. It artificially suppresses the development of flow separation, predicts a delayed separation position and yields a smaller separation scale. When the angle of attack further increases to 26.196°, large-scale flow separation emerges over the wing surface, accompanied by prominent unsteady vortex shedding in the wake. DynIDDES fully captures the whole process of shear layer roll-up, breakdown and wake shedding, as well as the features of early separation and expanding vortex instability regions. RANS, by contrast, is constrained by inherent over-modelling, which suppresses unsteady flow fluctuations. This not only delays separation growth and narrows the separation zone, losing fine flow field details, but also distributes surface pressure improperly. Such deviations in flow field and pressure distribution eventually induce noticeable discrepancies in predicted aerodynamic forces and pitching

moments.

Figure 6 compares the time-averaged and instantaneous surface pressure distributions from RANS and DynIDDES at typical angles of attack.

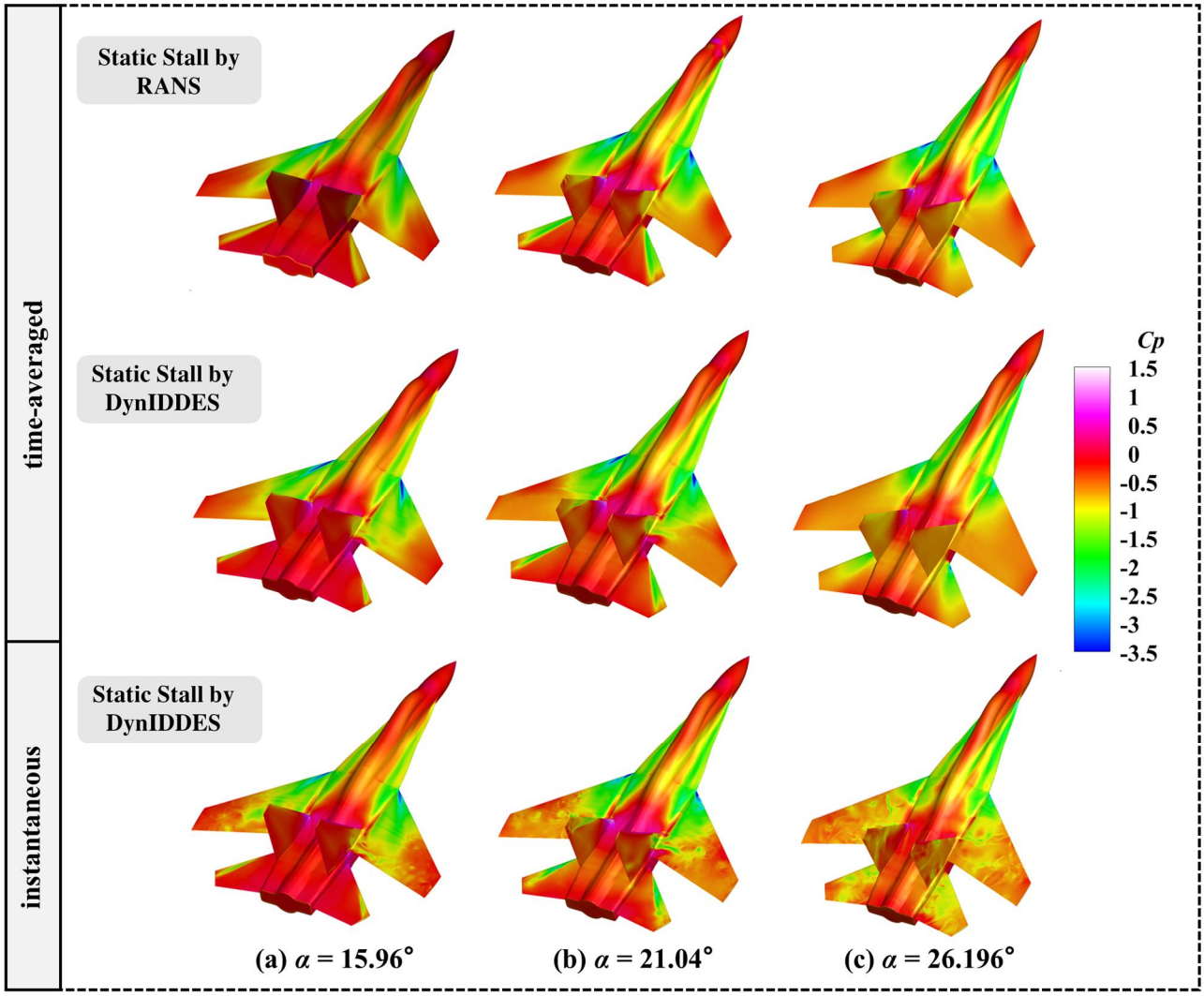


Fig. 6 Comparison of time-averaged and instantaneous surface pressure distributions predicted by RANS and DynIDDES at typical angle-of-attack conditions.

At 15.96°, the two methods yield broadly similar time-averaged pressure fields. The flow remains dominated by attached flow, with the negative pressure zone concentrated near the wing leading edge and minor discrepancies in mean pressure results. Their instantaneous pressure distributions also follow nearly identical overall patterns for the main negative pressure area on the suction surface, yet DynIDDES captures more local discreteness and non-uniformity over the wing and trailing edge, which marks the initial unsteady evolution of the leading-edge vortex.

As the angle of attack rises to 21.04° and 26.196°, the negative pressure zone expands spanwise and three-dimensional separation becomes increasingly intense. In terms of time-averaged results, DynIDDES better resolves spanwise pressure non-uniformity and sharp local pressure gradients, reflecting pressure redistribution caused by separated vortex instability and expanding separation zones. Affected by numerical dissipation, RANS fails to fully characterize intensified local pressure gradients and spanwise undulations, and overestimates leading-edge peak suction, leading to poor representation of pressure evolution during separation and vortex breakdown. Though both methods share consistent macroscopic pressure trends, they differ greatly in resolving local negative pressure ranges and fine pressure gradient features.

For instantaneous pressure fields at higher angles, DynIDDES captures strong unsteady pressure fluctuations across the wing, tail and fuselage, closely associated with leading-edge vortex entrainment, instability, breakdown and wake vortex shedding. With separation moving upstream and the separation range expanding rapidly, wake vortices produce a stronger coupling effect on

surface pressure. By contrast, RANS suffers from severe numerical smoothing and cannot capture the migration of separation and instantaneous vortex shedding. Such pressure deviations shift the aerodynamic load acting point, which further accounts for noticeable discrepancies in pitching moment predictions between the two methods. Overall, DynIDDES presents better performance in resolving both mean and instantaneous pressure features induced by unsteady separated flows.

Furthermore, to analyze the differences in the predictions of wall shear effects between the two methods, Fig. 7 shows the time-averaged wall shear stress distribution τ_n on the wing surface, and Table 1 lists the comparison results of the friction drag coefficient C_{d_f}.

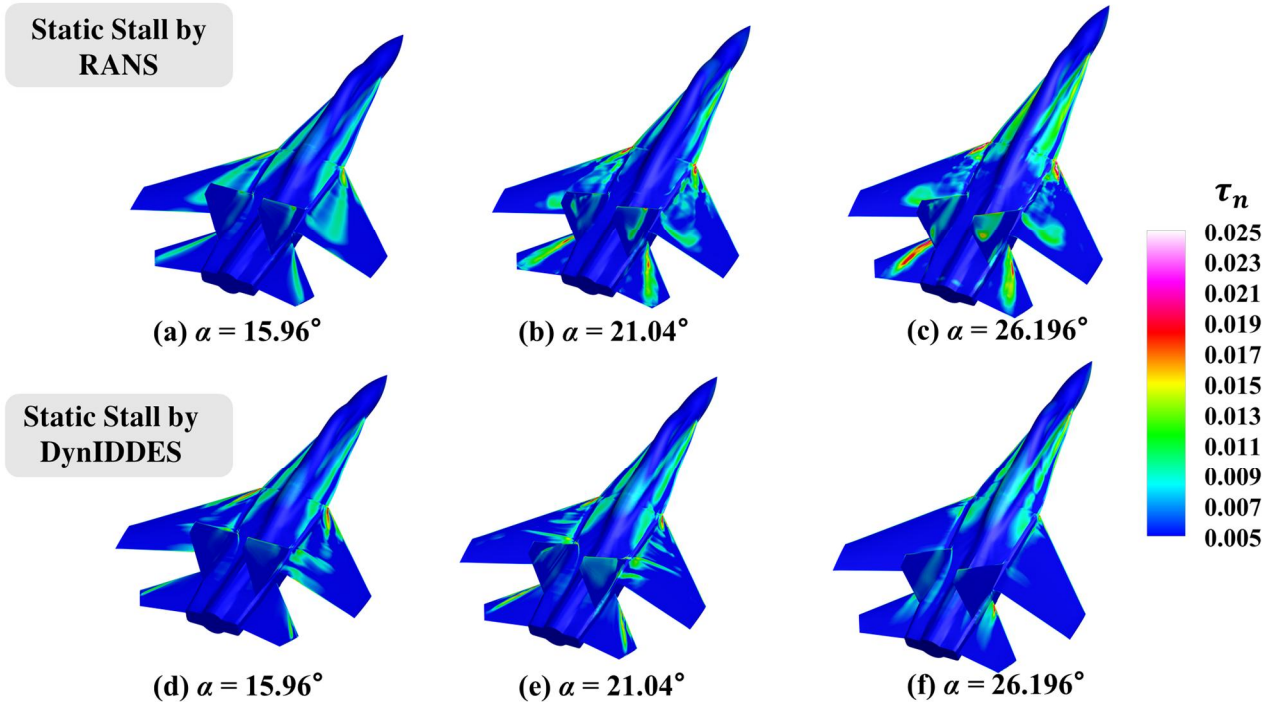


Fig. 7 Comparison of time-averaged wall shear stress distribution under typical angle of attack conditions.

Table 1 Comparison of C_{d_f} between RANS and DynIDDES under typical angle of attack conditions.

α /(°)	RANS	DynIDDES	Difference(%)
15.96	0.0156	0.01518	2.77%
21.04	0.016	0.0147	8.84%
26.196	0.01597	0.0131	21.9%

As shown in Fig. 7 and Table 1, at an angle of attack of 15.96°, the predicted wall friction drag coefficients by the two methods are generally similar, with a relative difference of only 2.77%. At this angle, the flow field is still dominated by adhering flow and local initial separation, with little difference in wall shear stress distribution. As the angle of attack increases, the differences in prediction between the two methods increase to 8.84% and 21.9%, respectively. Comparative analysis shows that DynIDDES can more precisely distinguish the wing vortex structure and its wall shear effect, calculating a significantly larger low-friction region, reflecting earlier flow separation initiation and more complete separation zone development. In contrast, the RANS method has higher numerical dissipation and a significant inhibitory effect on the expansion of the separated shear layer. It not only lags in predicting the separation location but also overestimates the extent of the surface adhering zone, ultimately leading to an overestimation of the predicted friction drag coefficient.

Combined with the drag coefficient variation pattern in Fig. 4, it can be seen that the total drag increase under high angle of attack conditions mainly comes from the pressure drag induced by separation. DynIDDES, by effectively analyzing the large-scale unsteady vortex structure in the separation region, more realistically reproduces the entire process of leading-edge vortex instability, premature separation, shear layer entrainment, and wake shedding, demonstrating higher accuracy in predicting surface pressure distribution and frictional drag characteristics. In contrast, RANS suffers from excessive dissipation in complex separation flows at high angles of attack, leading to

delayed separation development and an underestimated separation range, thus increasing the overall prediction error of aerodynamic forces at high angles of attack.

In summary, both turbulence methods exhibit high predictive accuracy under low angle-of-attack attached flow conditions; however, in high angle-of-attack strongly separated flow conditions, DynIDDES can more accurately capture the migration of separation positions and the evolution of unsteady flow field structures, significantly outperforming the traditional RANS method in both aerodynamic prediction accuracy and flow field detail analysis capability. This verifies the effectiveness and applicability of this method in numerical simulation of complex separation flows at high angles of attack for fighters.

4.2 Dynamic Stall Flow Simulation

This section focuses on the longitudinal forced pitching dynamic stall characteristics of the fighter model during rapid nose-up maneuver. The angle of attack varies continuously from 10.64° to 41.49° to reveal the unsteady aerodynamic hysteresis effect induced by dynamic flow separation and vortex evolution. Fig. 8 presents the schematic of this rapid pitch-up maneuver, while Fig. 9 contrasts the aerodynamic coefficients during dynamic pitching with the static counterparts to quantify their discrepancies.

It can be seen that the lift and drag coefficients of the dynamic condition are significantly higher than those of the static condition across the entire angle of attack range. Furthermore, the difference between the two gradually widens as the angle of attack increases, indicating that the rapid upward maneuver significantly enhances the unsteady effects in the flow field.

In the small to medium angle of attack range, the aerodynamic differences between the dynamic and static conditions are relatively small, and the flow is still dominated by attached flow or weakly separated flow. As the angle of attack enters the nonlinear region, due to the unsteady effects introduced by the pitching motion, the flow field exhibits a significant hysteresis response to changes in angle of attack. This causes the main vortex formed by the leading-edge separation shear layer to maintain strong coherence and a complete structure for a longer period, thus delaying the vortex breakup process. Compared to the static condition, the main vortex under dynamic conditions can maintain a strong suction effect over a wider angle of attack, creating a larger low-pressure area on the upper surface of the wing. This significantly increases the lift coefficient, exhibiting typical dynamic stall vortex lift enhancement characteristics. Simultaneously, as the angle of attack increases, the separation region expands rapidly, the unsteady vortex structure develops continuously, accompanied by more intense flow mixing and energy dissipation, leading to a significant increase in drag. Therefore, the drag coefficient under dynamic conditions is also significantly higher than that under static conditions, and the growth trend is more pronounced at high angles of attack.

Overall, rapid pitching maneuvers alter the generation, development, and breakup evolution of leading-edge vortices, causing the flow to exhibit typical dynamic stall characteristics. Due to the unsteady response hysteresis of the flow field, the leading-edge vortex can maintain structural stability at higher angles of attack under dynamic conditions, achieving enhanced vortex lift and stall delay, but this also induces stronger flow separation, resulting in a significant increase in aerodynamic drag.

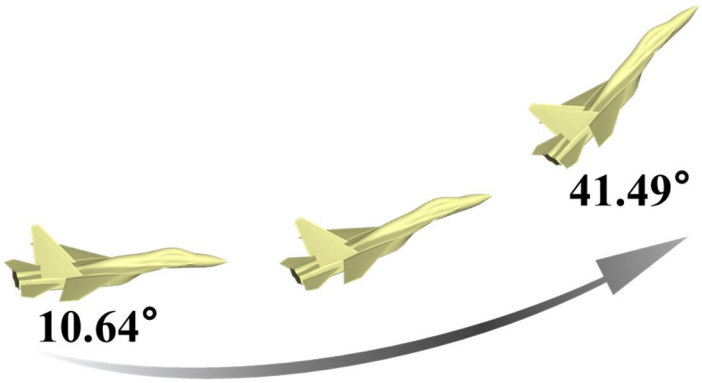


Fig. 8 Schematic diagram of forced pitch flight condition.

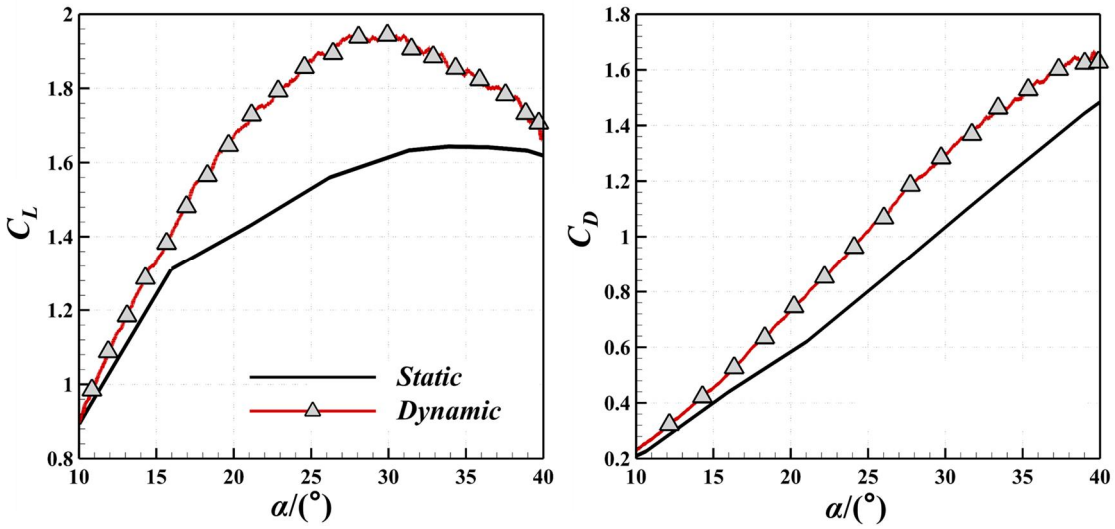


Fig. 9 Comparison of aerodynamic load coefficients under static and dynamic conditions.

Fig. 10 shows the typical flow field structures presdicted by DynIDDES under static and dynamic conditions at different angles of attack.

Distinct differences in flow field evolution are observed between static conditions and rapid pitching maneuvers in DynIDDES predictions. Under static conditions, the leading-edge vortex undergoes rapid destabilization and breakdown as the angle of attack rises. During rapid pitch-up motion, however, the leading-edge separated vortex retains strong coherence across a wider range of angles of attack. Its core breakdown is evidently delayed compared with the static case, presenting typical dynamic stall characteristics. The flow response lags behind the pitching motion, enabling the primary leading-edge vortex to stay fully developed over the wing upper surface. This further postpones vortex instability and breakdown and broadens the effective stall boundary. Meanwhile, large-scale vortical evolution in the wake becomes more prominent, which demonstrates that rapid pitching amplifies unsteady flow effects.

Such flow field discrepancies reveal the variations in aerodynamic performance between the two flow states. The flow lag keeps the leading-edge vortex generating strong suction at higher angles of attack, which improves vortex lift and delays stall. The expanded separation zone and complex wake vortices also lead to increased pressure drag. Overall, DynIDDES well captures the unsteady evolution of separated vortices under static and dynamic high-angle-of-attack conditions, and reasonably clarifies the flow mechanisms behind aerodynamic load variations during dynamic stall.

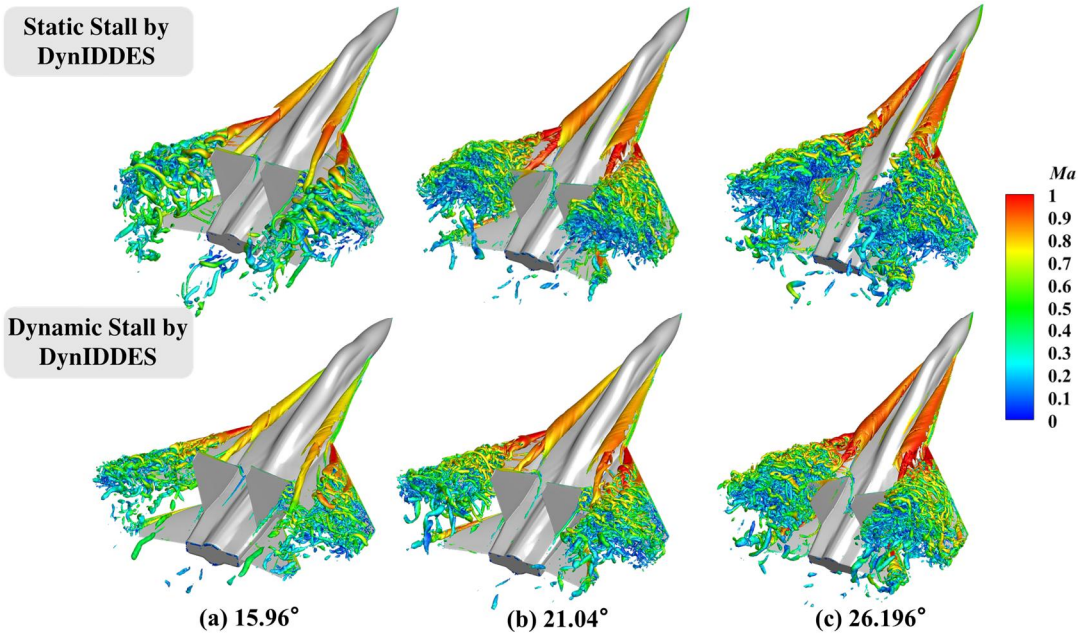


Fig. 10 Comparison of analytical capabilities of flow field structure under static and dynamic conditions at different angles of attack (Rortex = 40)

5. Conclusion

This paper adopts URANS and DynIDDES turbulence simulation methods to perform numerical investigations on static high-angle-of-attack stall and longitudinal dynamic pitch-up stall of a scaled fighter model. In terms of aerodynamic force and moment predictions, DynIDDES achieves better agreement with wind tunnel test data than RANS. Further comparison reveals distinct differences between the two approaches in resolving multi-scale separated vortical structures. Since RANS relies on temporal averaging, it filters out unsteady flow fluctuations and suffers from severe numerical dissipation of local flow details under strong separation. In contrast, DynIDDES integrates the merits of RANS and LES, enabling it to reasonably reproduce unsteady flow features including leading-edge separation, vortex instability and wake evolution. This method also well captures the spatial evolution of surface pressure redistribution and wall shear variation, and characterizes the aerodynamic hysteresis during forced-pitch dynamic stall, such as sustained vortex coherence, delayed vortex breakdown and an expanded stall boundary.

Acknowledgements

The research was supported by the National Natural Science Foundation of China (No.U23B6009, and No.U2570218). The computations were conducted in Computing Center in Xi'an. The authors thankfully acknowledge these institutions.

Copyright Statement

The authors confirm that they, and/or their company or organization, hold copyright on all of the original material included in this paper. The authors also confirm that they have obtained permission, from the copyright holder of any third party material included in this paper, to publish it as part of their paper. The authors confirm that they give permission, or have obtained permission from the copyright holder of this paper, for the publication and distribution of this paper as part of the ICAS proceedings or as individual off-prints from the proceedings.

References

[1] Wang N, Ma R, Chang X, et al. Numerical virtual flight simulation of quasi-cobra maneuver of a fighter aircraft[J]. Journal of Aircraft, 2021, 58(1): 138-152.

[2] Zhao Zhigao, Li Yan, Zhang Shuguang. Influence analysis on key parameters for aircraft maneuverability effectiveness evaluation[J]. Aeronautical Science & Technology, 2022, 33(08): 41-50.

[3] WANG X, WANG X, et al. Aerodynamic modeling and flight simulation of maneuver flight at high angle of attack[J]. Acta Aeronauticaet Astronautica Sinica, 2023, 44(19): 128410.

[4] WANG Haifeng, ZHAN Jingxia, CHEN Ke, et al. Development and application of aerodynamic research technologies for fighters at high angle of attack[J]. Acta Aerodynamica Sinica, 2022, 40(1): 1-25.

[5] Brandon J M. Dynamic stall effects and applications to high performance aircraft[J]. Aircraft Dynamics at High Angles of Attack: Ezperiments and Modelling, 2003, 19910012793.

[6] Kaifeng H E, Gang L I U, Zhongjun M A O, et al. Model flight test technology for post-stall maneuver of advanced fighter[J]. Acta Aerodynamica Sinica, 2021, 38(1): 9-20.

[7] YANG X M, LIU N, GUO CP, et al. A survey of aeroelastic wind tunnel test technology of flight vehicles[J]. Acta Aerodynamica Sinica, 2018, 36(6): 995-1008.

[8] LI Q Y, LI G, WEI Y T, et al. Review of aeroelasticity design for advanced fighters[J]. Acta Aeronautica et Astronautica Sinica, 2020, 41(6): 37-63.

[9] WU Jifei, KONG Wenjie, LI Guoshuai, et al. Progress and prospect on Reynolds number effects of advanced aircraft[J]. Acta Aerodynamica Sinica, 2024, 42(8): 3559.

[10] Wang N, Ma R, Chang X, et al. Numerical virtual flight simulation of quasi-cobra maneuver of a fighter aircraft[J]. Journal of Aircraft, 2021, 58(1): 138-152.

[11] SHU B W, DUYM, GAOZH, et al. Numerical simulation of Reynolds stress model of typical aerospace separated flow[J]. Acta Aeronautica et Astronautica Sinica, 2022, 43(11): 526385.

[12] MENG D H, SUN Y, WANG Y T, et al. Numerical simulation of fluctuating pressure of fighter vertical tail[J]. Acta Aeronautica et Astronautica Sinica, 2016, 37(8): 2472-2480.

[13] Quanzheng Li, Xiaoyu Sun, Gang Wang. Detached-eddy Simulation of the Vortex System on the High-Lift Common Research Model[J]. Physics of Fluids, 2024, 36:025173.

[14] Yang S, Chen P C, Wang X, et al. Prediction of buffet loads of F-15 with FUN3D solver[C]//54th AIAA Aerospace Sciences Meeting. 2016: 0305.

[15] Spalart P R. Comments on the Feasibility of LES for Wings and on the Hybrid RANS/LES Approach[C]//Proceedings of the First AFOSR International Conference on DNS/LES. 1997: 137-147.

[16] Shur M L, Spalart P R, Strelets M K, et al. A hybrid RANS-LES approach with delayed-DES and wall-modelled LES capabilities[J]. International journal of heat and fluid flow, 2008, 29(6): 1638-1649.

[17] Li Q, Chen X, Wang G, et al. A dynamic version of the improved delayed detached-eddy simulation based on the differential Reynolds-stress model[J]. Physics of Fluids, 2022, 34(11).

[18] M. ZHU, S. WANG, J. CAI, W. LIU. Simplified Reynolds-stress model based detached eddy simulations in fixed coordinate system[J]. Chinese Journal of Aeronautics, 2026, 104146.

[19] Wang G, Li Q, Sun X. Resolution assessment of Reynolds stress model-based DES methods for high-lift device flow over 30P30N configuration[J]. Aerospace Science and Technology, 2024, 145: 108863.

[20] Tu Z, Zhong B, Qi Y, et al. Study on Aerodynamic Characteristics of DLR-F4 Wing–Body Configuration Using Detached Eddy Method Incorporated with Fifth-Order High-Accuracy WENO/WCNS[J]. Aerospace, 2025, 13(1): 2.

[21] SI H Q, DONG H, et al. Verification and validation of deep dynamic stall numerical simulation method[J]. Acta Aeronautica et Astronautica Sinica, 2026, 47(6): 132671.

[22] Xing Haonan, Zhao Huan, Gan Yujie, et al. Analysis of dynamic stall characteristics of rotor airfoil in pitching motion state[J]. Acta Aerodynamica Sinica, 2026, 44(X): 1-16.

[23] Wang G, and Ye Z Y. Mixed element type unstructured grid generation and its application to viscous flow simulation. 24th International congress of aeronautical sciences, Yokohama, Japan, Vol. 1, ICAS 2004-2.4 (St.).R.3, pp 1-8, 2004.

[24] Wang G, Zhang T, Lin T, et al. Investigation of flight stability for fixed canard dual-spin projectile via CFD/RBD coupled method[J]. Defence Technology, 2025, 53: 1-18.

[25] Wang G, Liu Z K, Liu Y L, et al. Similarity laws for single-nozzle retropropulsion flow structures in reusable launch vehicles[J]. Physics of Fluids, 2026, 38(4).

[26] National Space Science Data Center (NSSDC), China. Verification and Validation Database of Computational Fluid Dynamics [EB/OL]. Available: https://nnw-vvdb.nssdc.ac.cn.

[27] LIU C Q. Liutex-third generation of vortex definition and identification methods[J]. Acta Aerodynamica Sinica, 2020, 38(3): 413-431.